Main-ion Intrinsic Toroidal Rotation Across the ITG/TEM Boundary in DIII-D Discharges During Ohmic and Electron Cyclotron Heating

B. A. Grierson,[1,*] C. Chrystal,[2] S.R. Haskey,[1] W.X. Wang,[1] T.L. Rhodes,[3] G. R. McKee,[4] K. Barada,[3] X. Yuan,[1] M.F.F. Nave,[5] A. Ashourvan,[1] and C. Holland[6]

[1]*Princeton Plasma Physics Laboratory, Princeton University, Princeton, NJ 08543, USA*
[2]*General Atomics, P.O. Box 85608, San Diego, CA 92186-5608, USA*
[3]*Department of Physics and Astronomy, University of California, Los Angeles, California 90095, USA*
[4]*Department of Engineering Physics University of Wisconsin-Madison, Madison, WI 53796, USA*
[5]*Associacao do Instituto Superior Tecnico para a Investigacao e Desenvolvimento, P1049-003 Lisbon, Portugal, Instituto de Plasmas e Fusao Nuclear, Instituto Superior Tecnico, Universidade de Lisboa, P1049-001 Lisbon, Portugal*
[6]*University of California San Diego, 9500 Gilman Dr., La Jolla, CA 92093-0417*

(Dated: March 23, 2019)

Direct measurements of deuterium main-ion toroidal rotation spanning the linear ohmic to saturated ohmic confinement (LOC-SOC) regime and with additional electron cyclotron heating (ECH) are presented and compared to the more commonly measured impurity (carbon) ion rotation in DIII-D. Main ions carry the bulk of the plasma toroidal momentum, and hence the shape of the main-ion rotation is more relevant to the study of angular momentum transport in tokamaks. In both the linear ohmic confinement (LOC) regime and with ECH, the main-ion toroidal rotation frequency is flat across the profile from the sawtooth region to the plasma separatrix. However, the impurity rotation profile possess a rotation gradient, with the rotation frequency being lower near the plasma edge, implying a momentum pinch or negative residual stress inferred from the impurity rotation that differs from the main-ion rotation. In the saturated ohmic confinement regime (SOC), both the main-ion and impurity rotation profiles develop a deeply hollow feature near mid-radius while maintaining the offset in the edge rotation, both implying a positive core residual stress. In the radial region where the rotation gradient changes the most dramatically, turbulence measurement show that density fluctuations near the TEM scale are higher when the rotation profile is flat, and drop significantly when the plasma density is raised and the rotation profile hollows, consistent with instabilities damped by collisions. Linear initial value gyrokinetic simulations with GYRO indicate the transition from LOC-SOC in DIII-D occurs as trapped electron modes (TEMs) are replaced by ion temperature gradient driven modes (ITGs) from the outer radii inwards as the plasma collisionality increases, $Z_{\rm eff}$ decreases, and the power flow through the ion channel progressively increases due to the electron-ion energy exchange. Gyrofluid modeling with TGLF successfully reproduces the plasma profiles at key times in the discharge, and in time dependent simulations with predictive TRANSP. TGLF indicates that during the LOC and SOC regimes as well as with ECH, subdominant modes are present and that the plasma is not in a pure TEM or ITG binary state, but rather a more subtle mixed state. Predictions of the main-ion rotation profiles are performed with global nonlinear gyrokinetic simulations using GTS and reveals that the flat rotation is due to oscillatory variation of the turbulent residual stress across the profile, whereas the deeply hollow rotation profile is due to a larger-scale, dipole-like stress profile. In these cases, the predicted and observed main-ion rotation profile is consistent with the balance of turbulent residual stress and momentum diffusion.

PACS numbers: AA.bb

I. INTRODUCTION

In axisymmetric tokamaks the plasma has been observed to develop a self-generated net rotation, as well as shear in the rotation profile, both in absence of applied torques. This 'intrinsic rotation' is a curious and fascinating phenomena in transport physics, as it so clearly deviates from a Fick's law type of gradient driven momentum transport. The desire to understand and even control this intrinsic rotation is not simply an academic pursuit, but indeed has practical implications.

As the size of fusion reactors such as ITER greatly exceed the size of current machines, the ability to drive toroidal plasma rotation from high power high voltage

*Electronic address: bgriers@pppl.gov

neutral beam injection (NBI) accordingly decreases with the greater moment of inertia. Therefore, understanding the fundamental mechanisms by which intrinsic rotation is generated, and how those processes scale to future machines is needed.

There is a number of ways in which the intrinsic rotation is important. First, near the plasma edge, self-generated co-current toroidal rotation acts to lift the plasma radial electric field E_r sufficiently high that the profile of E_r crosses zero in the vicinity of the pedestal top. It has been widely observed experimentally that a zero crossing of quantities related to the electric field ($\mathbf{E} \times \mathbf{B}$ rotation, electron perpendicular fluid rotation) near the pedestal top is associated with achieving suppression of edge localized modes (ELMs)[1, 2]. Second, in the plasma core the intrinsic rotation profile has been observed to take on either negative or positive gradients, producing a profile that is either peaked or hollow. When the toroidal rotation profile is hollow it can even cross zero, and be negative in the deep core while maintaining a co-current edge rotation. Achieving and sustaining differential plasma rotation is important for MHD stability, as differential rotation can inhibit the phase locking of magnetic islands and triggered coupling of sawteeth, tearing modes and ELMs, which can lead to a disruption[3]. Depending on the tendency of the plasma to form a peaked or hollow rotation profile, the plasma may either either work with, or against, any imparted torque from NBI. Finally there is the fundamental link between toroidal rotational shear, shear in the $\mathbf{E} \times \mathbf{B}$ rotation, and turbulence suppression. The working hypothesis presented in this article is that the shear developed in the intrinsic toroidal plasma rotation is driven by turbulent transport in the long wavelengths on the order of the ion sonic Larmor radius ρ_s. It is this long wavelength turbulence that produces most of the thermal, particle and momentum "anomalous" transport that degrades plasma confinement, and which is most effectively stabilized by $\mathbf{E} \times \mathbf{B}$ producing improving confinement[4]. Hence it is logically inconsistent that the plasma can fully quench the turbulence through a turbulence-driven mechanism. Gain in the plasma energy confinement produced by turbulence-driven intrinsic rotation gradients will depend on the relative momentum to energy transport ratio (the Prandtl number), which is of order unity, indicating that shear suppression of turbulent transport by intrinsic rotational shear should be small. However, clear confinement improvements have been observed in the Alcator C-Mod tokamak[5] through a synergy of the intrinsic plasma rotation and heating in the ion cyclotron resonance frequency (ICRF) range. Furthermore, there are many off-diagonal transport mechanisms in plasmas, and multi-channel effects between particle, thermal and momentum transport are not unexpected. These considerations motivate investigations to understand the types of turbulence producing rotation shear, and how these mechanisms scale.

In this article, we investigate the intrinsic plasma rotation of main-ions and impurities in the DIII-D tokamak[6], which is equipped with a flexible shaping capability, neutral beam injection (NBI) and electron cyclotron heating (ECH) systems. With these DIII-D experiments we add to a body of literature recently reviewed[7] on measurements and modeling of toroidal rotation reversals, across what are categorized as Type-I reversals where the plasma undergoes a change from co-current to counter-current central toroidal rotation as the density is increased, resulting in a "hollow" profile above a critical density. A key advancement for studying plasma rotation in DIII-D has been the recent capability to measure the bulk plasma rotation directly. In nearly all of the reviewed literature on intrinsic plasma rotation[7–11],the ion flow that is measured and reported is the impurity rotation; some key examples in helium plasmas do exist[12]. This main-ion charge exchange recombination (CER) spectroscopy measurement on DIII-D was initially performed in the plasma core, and recently extended to a full profile including high resolution edge measurements[13–18]. Direct measurements of the main-ions is critical, as most previous studies have relied on measuring trace impurities, and either performing neo-classical corrections to the impurity measurements, or simply assuming that the impurity and main-ion rotation are the same.

In this article we will use a well known plasma phenomenon of the linear ohmic confinement (LOC) to saturated ohmic confinement (SOC) transition[19, 20] achieved by varying the plasma density, and inducing a toroidal 'rotation reversal' in the plasma core between co-current and counter-current directions. The article is organized as follows: Sec II introduces the LOC-SOC transition and describes the experimental conditions and observation of the LOC-SOC transition in recent DIII-D experiments. Comparisons between main-ion deuterium and impurity carbon profiles will be shown in Sec III. Also in Sec. III we highlight the even *qualitatively* different conclusions about the momentum transport physics inferred from the profiles themselves, and potential misleading interpretations when only impurity measurements are available. We also show that adding electron heating to a low density plasma with de-coupled electrons and ions does not cause a rotation profile hollowing, and later shown to be consistent with power through the ion channel being associated with the ITG mode and rotation reversal. We apply turbulence modeling in three stages, focusing on linear initial value gyrokinetics in Sec. IV to assess the dominant linear instability We then use TGLF for transport flux-matching and linear dominant and sub-dominant eigenvalues in Sec. V, and finally nonlinear global gyrokinetics with GTS to explore the generation of residual stresses from symmetry breaking mechanisms in Sec. VI. The progression of modeling results show that the low density LOC condition with flat rotation profile is near an ITG/TEM transition, with linear initial value GYRO simulations indicting TEM, but flux-matched TGLF indicating ITG with sub-

dominant TEM. In the low density LOC with additional ECH, both GYRO and TGLF indicate that the regime is dominated by TEM instabilities across the plasma radius, with TGLF indicating sub-dominant ITG. The high density condition displays a low-k spectrum with dominant ITG modes where the reversal occurs near $\rho \approx 0.6$, but an increasing fraction of TEM instability with increasing radius, and highlights a more complex picture than a broad characterization of ITG vs. TEM dominant. Finally, predictive TRANSP with TGLF is used to show that the thermal transport across the LOC-SOC transition in DIII-D can be achieved via time-dependent simulation in a manner similar to Ref. [21], and opens the opportunity for integrated simulations of low-torque plasma conditions where residual stress is an important contribution to momentum flux and the achievable plasma rotation. We then conclude and discuss open issues and continuing activities.

II. ACHIEVING THE LOC-SOC TRANSITION IN DIII-D

A confinement transition under ohmic heating from a monotonically increasing thermal energy confinement with increasing density, to a saturated energy confinement independent of density has been studied for many years in tokamaks. It was long speculated that the confinement transition occurred due to the onset of anomalous ion thermal transport. This explanation begins with a low density plasma and the logic follows from the fact that ohmic tokamak operation produces direct electron heating and indirect ion heating. At low density, the ions and electrons are thermally decoupled and electron energy confinement is poor compared to ion energy confinement. As one raises the density, an increasing fraction of the power flows through the ion thermal transport channel, because the ion-electron energy exchange (equipartition flux) is proportional to $n_e^2(T_e - T_i)/T_e^{3/2}$. This preferentially raises the stored energy per unit ohmic power as the ions (with better energy confinement) become heated. The critical break in rising energy confinement then occurs as sufficient power flows through the ion channel to produce ion temperature gradient (ITG) driven turbulence. Due to the stiff thermal transport for both ion and electron energy fluxes associated with ITG modes, increased ohmic heating cannot raise the temperature gradients or stored energy. This explanation has matured to the present understanding that the low density conditions are dominated by trapped electron modes (TEM), which are stabilized by collisional electron de-trapping, and that the confinement transition occurs at a critical plasma collisionality. Furthermore, the role of impurities has been identified as stabilizing to ITG modes at low electron density with main-ion dilution and elevated $Z_{\rm eff}$, while at high electron density and high plasma purity ITG modes are more easily destabilized. There are many fascinating transport phenomena associated with the confinement transition, most importantly to this article being the "rotation reversal", which have been described and reviewed in great detail by Rice *et. al.*[20]. The subtleties of this turbulence instability interpretation are (i) the accuracy with which experiments can be diagnosed with equilibrium reconstruction, profile gradients, power balance and turbulence diagnostics, (ii) the fidelity of the gyrokinetic turbulence codes in computing the dominant and sub-dominant linear instabilities, nonlinear turbulent state, and satisfaction of the validation hierarchy[22]. At present, detailed linear and nonlinear turbulence modeling results from Alcator C-Mod tokamak are indicating that the rotation reversal occurs when the ITG mode is the dominant transport mechanism[23]. In fact, stabilization of the ITG instability by nitrogen seeding has been demonstrated to cause the hollow rotation profile to re-flatten[24]. In contrast, on the ASDEX-Upgrade tokamak is has been reported that the rotation reversal occurs very near the TEM to ITG transition based on linear stability considerations at a representative wavenumber, but slightly on the low collisionality side of the transition where TEM is dominant[25, 26]. In later sections of this article we present gyrokinetic and gyrofluid modeling of the dedicated discharges described next, and show that the landscape of the linear turbulence stability evolves in space and wavenumber between TEM and ITG modes, and more insight can be obtained by constructing a 2D map in space and wavenumber.

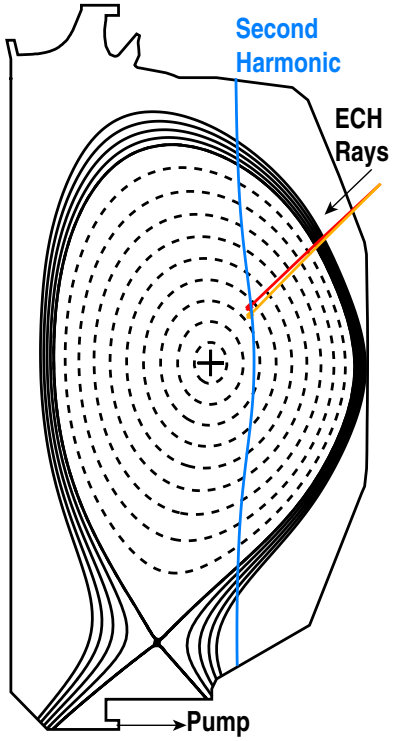

FIG. 1: Equilibrium used in DIII-D experiments chosen to match the shape of JET. Two ECH rays are shown for applying additional auxiliary heating for a sub-set of the experimental conditions.

On DIII-D, we first achieve the LOC-SOC transition in the classic way of systematically increasing the plasma density during a discharge under ohmic heating. This allows the determination of the transition density for the given plasma equilibrium for more detailed study. The plasma configuration is shown in Fig. 1 and is a lower single null (LSN) shape chosen to match JET for a joint isotope scaling experiment that will be described elsewhere in the future. The toroidal field is clockwise when viewed from above with $B_t \approx -2$ T and the plasma current is counter-clockwise when viewed from above with $I_p \approx 1$ MA. Also shown in Fig. 1 is the aiming of two gyrotrons used to apply additional electron heating in the late phase of a discharge described later. During these experiments, the plasma density is controlled with deuterium gas puffing feedback using line-averaged density measured by a multi-color CO2 interferometer. Multipoint measurements of the electron density and temperature are obtained with Thomson scattering, and electron cyclotron emission (ECE) is also used for electron temperature. Power radiated by the plasma is determined from tomographic inversion of a dual-view foil bolometer system. During the ohmic plasma operation, short pulses from the DIII-D NBI systems are used for measuring the properties of the main-ions and impurities from CER, as well as providing motional Stark effect (MSE) polarimetry for measuring the magnetic field pitch angle used in equilibrium reconstruction and constraining the equilibrium safety factor q. The NBI pulses are spaced sufficiently far apart that the fast-ions have fully decayed and their influence on the next measurement is absent, as calculated by TRANSP[27–29] with NUBEAM[30], providing up to six profiles during the plasma current "flat top" duration.

Identification of the LOC-SOC transition is shown in Fig. 2(a) that displays the thermal energy confinement time as a function of the volume averaged electron density computed with TRANSP. For this calculation the equilibrium and electron plasma profiles were reconstructed every 5.0 ms between 905-4000 ms. Ion profiles were reconstructed every 400 ms during NBI and linearly interpolated in time with TRANSP. Energy confinement time values are quoted during times at which the volume integrated NBI heating of ions and electrons, as well as the d/dt "gain" contribution to power balance has been reduced below 75 kW, which is less than 10% of the approximate 1 MW of ohmic power. In Fig. 2(a) it is observed that the extrapolated energy confinement does not pass through zero at zero plasma density. We attribute this to the fact that the early density is recorded during the plasma current ramp-up where the current and density are evolving together. We speculate that systematic error in the slow evolution of the power balance $\partial W/\partial t$ may be artificially reducing the energy confinement time, which can move the zero of τ_e to positive density.

Near the LOC-SOC transition density during the current flat top shown in Fig. 2(a) we observed the expected reversal of the toroidal rotation gradient of the carbon impurities, shown in Fig. 2(b). Here we use the definition of the normalized rotation gradient as $u' = -(R^2/c_s)d\Omega/dr$, where R is the geometric major radius, c_s is the ion sound speed, Ω is the toroidal ion rotation frequency, and r is the geometric minor radius. The value of effective collision frequency $\nu_{\rm eff}$ where the rotation reversal occurs is near $\nu_{\rm eff} \approx 0.4 - 0.7$, which is consistent with AUG[26], and near $\nu_{\rm eff} \approx 0.3 - 0.4$ found on Alcator C-Mod[31]. Here $\nu_{\rm eff}$ is the electron collision frequency normalized to the thermal transit time evaluated locally as in [26] for $\rho = 0.6$ In this plasma condition, the collisionality $\nu*$ is higher than $\nu_{\rm eff}$ by a factor of 1.4, making the range of $\nu*$ for the reversal between 0.5-1.0.

In the next section, we will focus on a density ramp-down discharge in a narrow range of density around the reversal, apply auxiliary power in low density showing that it does not affect the core rotation, and contrast main-ion and impurity rotation profiles.

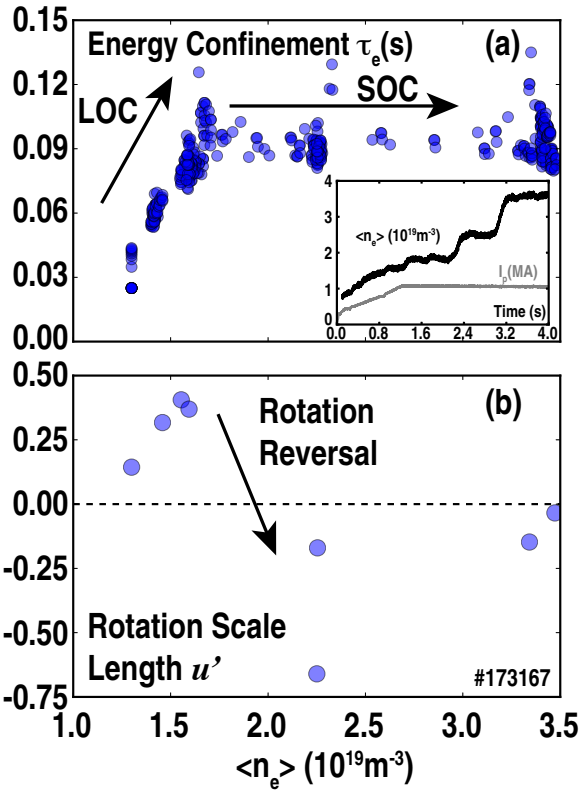

FIG. 2: Observation of the LOC-SOC confinement transition achieved by a density ramp-up discharge with only ohmic heating. (a) Energy confinement time calculated from measured plasma profiles using TRANSP with time history of plasma density (inset). (b) Carbon rotation gradient scale length u' at mid-radius

III. ROTATION PROFILE EVOLUTION DURING SLOW DENSITY RAMP-DOWN

Due to the relatively narrow region of density across which the rotation reversal occurs ($n_e \approx 1.5 - 2.0 \times 10^{19}$ m^{-3}), a discharge was executed in the opposite manner of the classic LOC-SOC density ramp-up by initiating the discharge at high density, and allowing the density to slowly decay naturally. A similar study of an ohmic reversal was studied on MAST[32] that achieved a rotation reversal from negative to positive. As seen in Fig 1 the lower divertor legs are not entering the pump duct, and this produces poor pumping efficiency and a slow decay of the plasma density in time. Allowing density to decay on a long timescale is more advantageous for studying the density sensitivity of the rotation reversal in DIII-D because this eliminates oscillations in the gas puffing feedback system that occur when the density is increased step-wise. During the discharge, evolution of the wall outgassing from the graphite tiles and changes in the confinement properties of the plasma can produce interactions with the density control systems, and these are eliminated by using the natural density decay. The density ramp-down discharge time history is shown in Fig. 3. Also shown in Fig. 3 are the indications of the neutral beam injection required for measuring the ion profiles, and the ECH power that is applied near the end of the discharge.

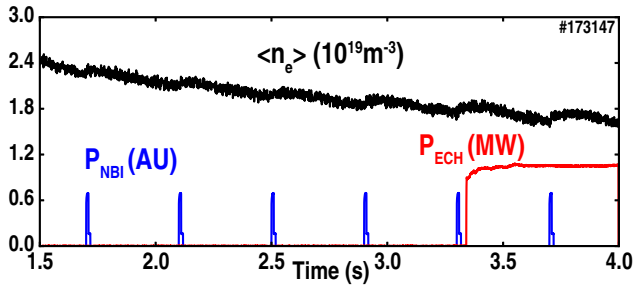

FIG. 3: Time evolution of a slow density ramp-down discharge on a narrow range of density near the LOC-SOC transition density shown in Fig. 2. Auxiliary heating from ECH is applied in the low density conditions in panel Fig. 2(a).

During the density ramp-down shown in Fig. 3 each neutral beam pulse provides a measurement of the ion profiles, most notably the toroidal rotation. Shown in Fig. 4(a-f) are the ion toroidal rotation profiles for both deuterium and carbon, taken as the first measurement point provided by the neutral beam at 2.5 ms CER time resolution, centered on the time integration window. The timestamp presented in the figure is the timestamp of the equilibrium reconstruction including MSE and pressure constraints, which are averaged over 10 ms (i.e. 1705 ms uses MSE from 1700-1710 ms). Rotation evolution occurs primarily between the $q = 1$ and $q = 2$ surfaces, which are located between $\rho \approx 0.4$ and $\rho \approx 0.70 - 0.75$.

There is a number of noteworthy differences between the main-ion and impurity rotation that have significance for interpreting the momentum transport responsible for establishing the profile. The framework for interpreting the rotation profile structure is well known and follows from the momentum balance equation, which is summed over ion species in an impure plasma, with inter-species flows related by the force balance equation. Evolution of the ion rotation profile is described by Eq. 1, with the transport flux represented by a decomposition in Eq. 2. Here in Eq. 1 Ω is the toroidal rotation, Π_φ is the radial flux of toroidal angular momentum and η_j is the local torque density for each source in summation.

$$m_i n_i \langle R^2 \rangle \frac{\partial \Omega}{\partial t} + \nabla \cdot \Pi_\varphi = \sum_j \eta_j \quad (1)$$

$$\Pi_\varphi = -m_i n_i \langle R^2 |\nabla \rho| \rangle \left(\chi_\varphi \frac{\partial \Omega}{\partial \rho} - V_p \Omega \right) + \Pi_{\rm resid} \quad (2)$$

In a static or slowly evolving discharge the momentum flux in the core Eq. 2 is zero ($\Pi_\varphi = 0$). Zero momentum flux is satisfied locally everywhere across the profile. In the limit of small momentum pinch V_p, one can easily see that the diffusive momentum flux and the residual stress balance. Hence, since χ_φ is positive definite, *the rotation gradient is directly proportional to the residual stress.* We will use this framework to interpret the observed rotation profiles in Fig. 4

Early in time with high density shown in Fig. 4(a), the central rotation profile is hollow. The main-ion rotation profile is zero near the axis and rises to a positive value achieving an approximately constant rotation frequency outside of $\rho \approx 0.7$. At this early time the impurity rotation profile is slightly negative near the magnetic axis, rises to achieve a local maximum near $\rho \approx 0.7$, and then falls monotonically by approximately a factor of two towards the separatrix. At the plasma separatrix, the main-ion rotation is approximately twice the impurity rotation. This difference in the edge rotation has been the focus of recent studies with mach probes observing the detailed features of the main-ion rotation near the separatrix[33, 34], and testing theory based models of momentum transport in the plasma edge producing net intrinsic rotation[35–37]. By interpreting the rotation profile gradients, we can immediately conclude that the hollow rotation profile inside of $\rho \approx 0.4 - 0.7$ is caused by either a positive residual stress, or an outward momentum pinch. However an outward pinch described in Refs. [38, 39] and tested in [40] is only theoretically possible with a hollow density profile. Therefore since $\Pi_{\rm resid} \propto \chi_\varphi \partial\Omega/\partial\rho$ we can directly infer that a positive residual stress momentum flux is required to form the positive rotation gradient between $\rho \approx 0.4 - 0.7$.

Both outside of $\rho \approx 0.7$ in Fig. 4(a-f) and later in time Fig. 4(e-f) are where the largest differences between the main-ions and impurities exist. Using the same logic as before, interpreting the flat main-ion rotation $\partial\Omega/\partial\rho \approx 0$ implies that either there is a very large momentum diffusivity or a negligibly small residual stress. If we only

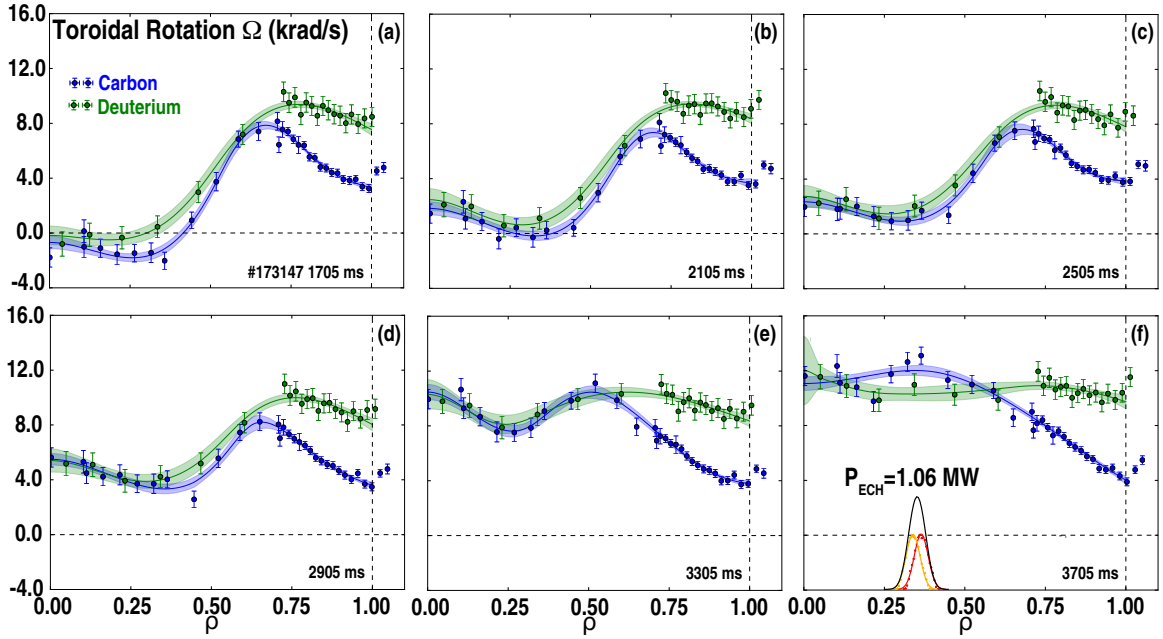

FIG. 4: Evolution of main-ion and impurity toroidal rotation profiles during the discharge shown in Fig. 3 as the density is slowly decreased

measured the impurity rotation profile, we would see that the profile is peaked everywhere, and would infer that since $\partial\Omega/\partial\rho < 0$ that there is either a negative residual stress or an inward pinch everywhere, together with a momentum diffusivity small enough that a gradient is observed. This contrast in interpreting the momentum transport highlights distinctly separate conclusions simply drawn from the profiles themselves. *Viewing only the impurity profile produces a misleading interpretation of the momentum transport physics.*

As time evolves in Fig. 4(b-e) the density is slowly lowered during only ohmic heating and the rotation profile hollowing slowly disappears. Finally in Fig. 4(f) the lowest density is presented, with additional electron heating by ECH. At this time the main-ion rotation hollowing disappears and the final rotation profile completely flat in the lowest density conditions. Here it is important to recognize that at low density, when the ions and electrons are most de-coupled, *adding electron heating does not cause a modification of the rotation profiles* (at higher density it has been widely reported that ECH modifies the intrinsic rotation[25, 41–43].) The only modification is a slight increase in the edge velocity that raises the entire profile with the boundary condition as the additional heating increases the separatrix ion temperature. This demonstrates that adding ECH in this low density plasma with decoupled ions and electrons does not modify the rotation profile, unlike higher density conditions where ECH increases the ion temperature and induces a rotation reversal[43]. The physics, as will be shown later, is related the heat flux through the ion channel being important for exciting ITG turbulence and producing the rotation reversal.

A. Thermal profile evolution

Measurements of the plasma profiles and inspecting derived quantities relevant to turbulent transport are a pre-requisite to interpreting the plasma transport or simulating the plasma instabilities. Here during the plasma density ramp-down and application of ECH shown in Fig. 3 , our goal is to move smoothly from an ITG to a TEM regime, and then once in the TEM regime we raise the electron temperature to lower the collisionality and move deeply into the TEM regime. Plasma profiles are reconstructed by first mapping to the diagnostic measurements in configuration space to the equilibrium flux map using the radial coordinate of ρ, defined as the square root of the normalized toroidal flux $\rho = \sqrt{\psi_t/\psi_{t,bdry}}$. All profile analysis and fitting has been performed using OMFIT[44] with the OMFITprofiles module[45] by using auto-knotted splines with least-squares minimization, where the number of knots are chosen based on the reduced χ^2. Equilibria and profiles were then used in TRANSP for confinement and power balance, and information transfer to the GACODE plasma modeling tools via OMFIT[46]. Shown in Fig. 5 are the plasma fluid quantities and derived quantities using the GYRO[47] convention.

During the density ramp-down the electron density profile shown in Fig. 5(a) exhibits a smooth reduction of the density magnitude, a small but continuous increase in the electron temperature in Fig. 5(b), until ECH is applied raising the temperature significantly for the 3705 ms timeslice, and a nearly constant ion temperature in Fig. 5(c). During ECH where the electron

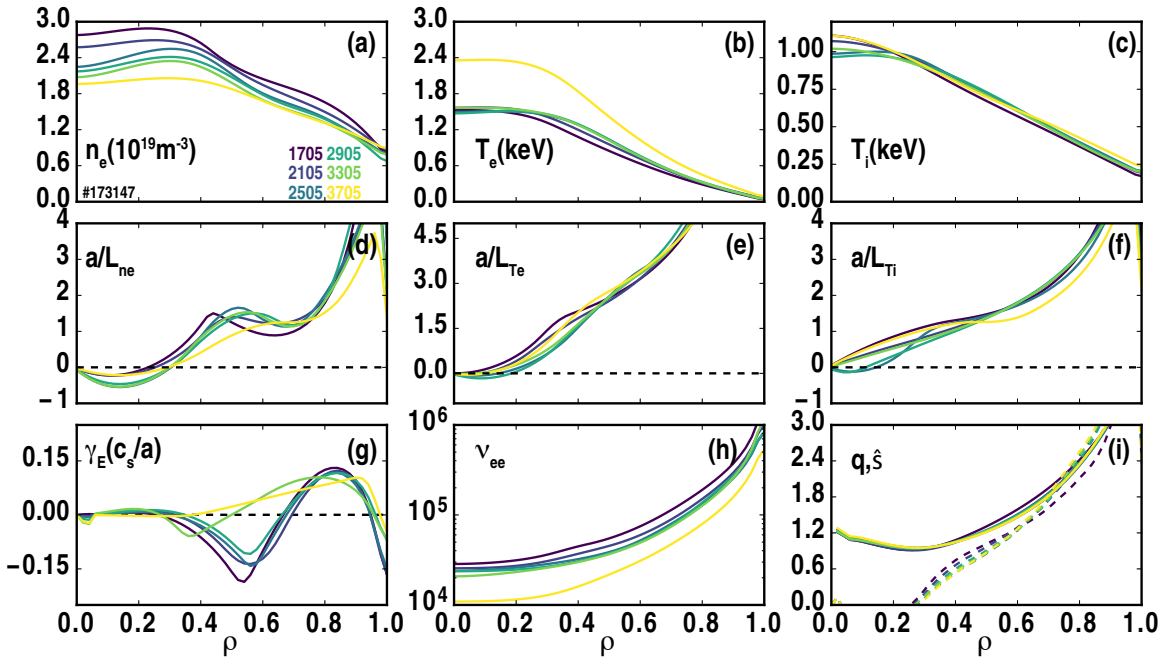

FIG. 5: Time evolution of thermal profiles during the slow density ramp-down discharge on a narrow range of density near the LOC-SOC transition density shown in Fig. 2 and rotation in Fig. 4. Shown are (a) electron density, (b) electron temperature, (c) ion temperature profiles and (d-f) normalized inverse scale lengths, (g) shear in the $\mathbf{E}\times\mathbf{B}$ rotation frequency, (h) electron-electron collision frequency and (i) q profile and shear (dashed). Auxiliary heating from ECH is applied in the low density conditions (t=3705 ms) to raise the electron temperature and reduce electron collisionality intended to achieve a TEM dominated turbulent state.

temperature is high we can see that the electron density peaking reduces, and that the ion temperature only increases in the outer half radius. Normalized inverse scale lengths, which both drive and react to to turbulent transport, have subtle but measurable systematic changes in the profile scale lengths ($a/L_X = -(a/X)(dX/dr)$) in Fig 5(d-f). Comparing early and later in time, we can see that the density profile curvature has evolved systematically from concave up to concave down, with the inverse scale length a/L_{ne} near $\rho = 0.6$ near unity. The electron temperature inverse scale length a/L_{Te} in Fig 5(e) systematically increases in time by a small amount, and the ion temperature inverse scale length a/L_{Ti} is nearly constant until ECH is applied, raising T_i at late time in the edge at nearly fixed gradient in Fig 5(f). One interesting correlation that has been reported earlier[48] is the structure of the density profile and the gradient in the plasma rotation, here represented by γ_E in Fig. 5(g). Although it is not easily resolvable here, contrasting the two extreme conditions at t=1705 ms vs. t=3705 ms we can see that the structure in the density and rotation gradients display the largest qualitative and related changes indicating a connection between the particle and momentum transport. The largest change in the quantities relevant to turbulent transport is the collision frequency, shown in Fig. 5(h), which clearly decreases in time as the density decreases and at the last time as ECH is applied to raise T_e. Finally, the equilibrium safety factor and magnetic shear as shown in Fig. 5(i) indicating that they do not change significantly in time in this low β_p plasma. One quantity that is also important to turbulence stability is the main-ion dilution and $Z_{\rm eff}$. In this condition, with a relatively narrow range of density variation, the $Z_{\rm eff}$ increases in time with reducing density, increasing from a profile-averaged $Z_{\rm eff} \approx 1.4$ to $Z_{\rm eff} \approx 1.55$.

B. Turbulence Measurements with Doppler Backscattering

The hypothesis is that the toroidal rotation profile is formed by a balance of turbulent transport and momentum diffusion, and that changes in the turbulence characteristics between the LOC-SOC regime is the underlying cause of the energy confinement saturation. Previous work on DIII-D using far infrared scattering had revealed an increase in low-k turbulence fluctuations across the transition from LOC to SOC regime, indicating the emergence of ITG turbulence[49]. Recent work on density fluctuations using a reflectometer in Tore Supra has revealed a quasi-coherent fluctuation in the plasma core while in the LOC regime where TEMs are robustly predicted to be unstable[50], and nonlinear gyrokinetic simulations have reproduced this observation. During the experimental discharge shown in Fig. 3 the DIII-D doppler backscattering (DBS) diagnostic was used to measure the

local density fluctuations in the intermediate-k range. Shown in Fig. 6 is the radial profile of the density fluctuations at three times in Fig. 3 corresponding to high density, low density before the application of ECH, and lowest density during ECH. In the outer radii of the plasma DBS is sensitivite to low-k instabilities $k_\theta \rho_s < 1$, whereas in the inner radii $\rho < 0.8$ the DBS measures fluctuations at the shorter wavelengths. In all conditions the plasma density fluctuations increase with major radius towards the plasma edge.

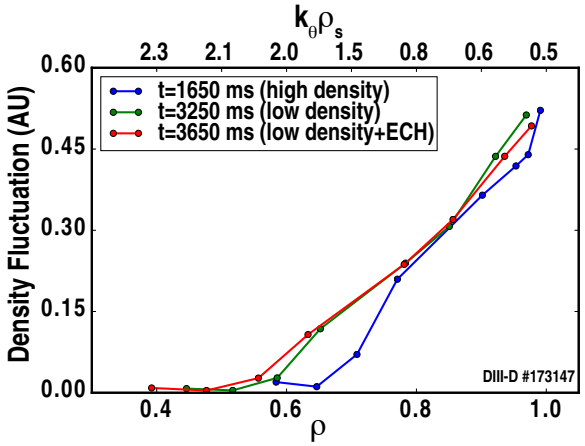

FIG. 6: Doppler backscattering of intermediate-k turbulence

Contrasting the high density and low density conditions reveals that at mid-radius in the region where the rotation profile is most strongly modified ($\rho = 0.4 - 0.8$), there is an increase in the electron density fluctuations in low density and low-density with ECH. It is noteworthy that the in low density the application of ECH does not produce a large increase in the turbulent fluctuations, and the EC waves produce effective electron heating in conditions where the ions and electrons are de-coupled, shown in Fig. 4(b). The lower fluctuation intensity at high density may indicate that the turbulence at this radius and wavenumber is damped by collisions, as the turbulence is weaker at high collisionality. In the outer regions of the plasma at low wavenumber, the fluctuations do not change significantly and may indicate that the type of turbulence in the outer radii is not changing in time or over this range of density.

C. Consistency with Force Balance and Neoclassical Poloidal Flow

In absence of direct main-ion toroidal rotation, one may invoke the radial force balance and calculated neoclassical poloidal flow to predict the main-ion rotation. This technique has been used in the past and has a fundamental reliance on the accuracy of the neoclassical poloidal rotation. We have shown in the past that the neoclassical modeling works best at high plasma collisionality[51], but not at low collisionality[52]. In these ohmic plasma conditions, here we show that the neoclassical modeling produces a reasonable approximation to the main-ion rotation across most of the profile. Using the neoclassical code NEO[53] we compute the main-ion and impurity poloidal flow velocity to predict the main-ion rotation, using the force balance for both ions with a common electric field similar to Refs. [14, 51]. Near the plasma edge there is reasonable agreement with NEO, as seen before[34]. Also, in the higher density condition in Fig. 7(a) the neoclassical approximation accurately captures the profile structure. Whether impurity rotation measurements, main-ion rotation measurements, or a neoclassical calculation of the main-ion rotation are used, the conclusion that the profile is indeed hollow are well satisfied. However, at low collisionality with ohmic and ohmic plus ECH presented in Fig. 7(b,c), respectively, the modeling is discrepant in the fact that NEO predicts a main-ion rotation profile with a significant rotation gradient. NEO predicts that the main-ion rotation is a near uniform positive offset from the impurity rotation in the mid and outer radii, and near the impurity rotation in the core where the pressure gradients are weak. In these cases, the evaluation of the main-ion rotation gradient from NEO is discrepant. This highlights the need for direct main-ion rotation measurements when inferring the mechanisms needed to explain the observed rotation (i.e. diffusion alone, pinch or residual stress).

IV. INITIAL VALUE LINEAR GYROKINETIC STABILITY WITH GYRO

Determining the dominant linear instability from initial value gyrokinetics provides insight into the expected transport phenomena associated with the linear modes, such as the thermal, particle and momentum transport and scaling with plasma parameters and drivers. As shown in Sec. III A during the plasma density rampdown the decrease of the electron density produces subtle changes in the driving profile gradients, but a larger variation in the plasma collisionality. Theoretically, at high density, high collisionality and plasma purity, the ITG mode can be de-stabilized and TEMs stabilized. As the density is lowered, main-ion plasma dilution increases and collisionality decreases, the TEM can dominate. In order to assess the fastest growing linear mode, the full physics gyrokinetic simulation code GYRO[47] has been used with experimental inputs shown in Fig. 5. Here GYRO simulations have been performed with experimental equilibrium, three kinetic species (electrons, deuterium and carbon), including electrostatic $\delta\phi$ and electromagnetic $\delta A_{||}$ fluctuations. Across the radial profile from $\rho = 0.45 - 0.8$ in steps of 0.05 and for binormal wavenumbers $k_\theta \rho_s = 0.1 - 1.0$ in steps of 0.05 we have performed linear initial value GYRO simulations to establish the dominant linear mode, shown in Fig. 8.

Three times from Figs. 3, 5 are simulated corre-

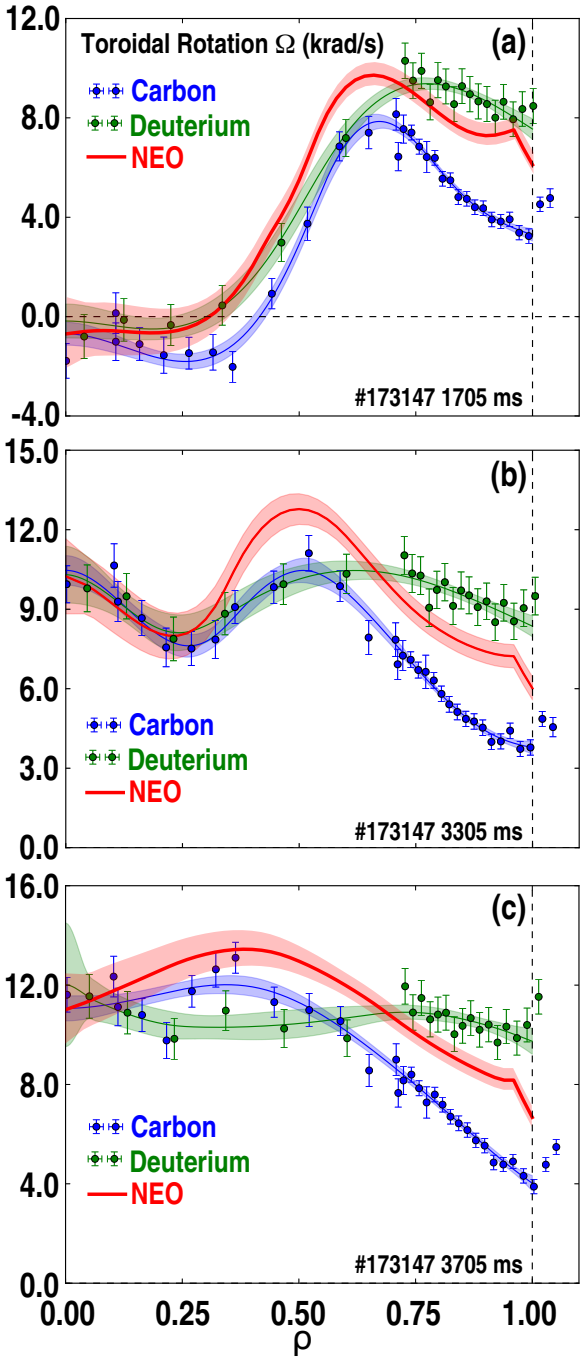

FIG. 7: Comparison between measured main-ion toroidal rotation and expected main-ion rotation calculated using radial force balance and poloidal flow from the neoclassical code NEO

sponding to the earliest time at highest density in Fig. 8(a,d), low density just before the application of ECH in Fig. 8(b,e) and lowest density including ECH in Fig. 8(c,f). In each pair of figures we show the growth rate of the most unstable mode γ, and the frequency ω of that mode, where negative frequency modes correspond to the ion diamagnetic drift direction. From these simulations, we can see that in the highest density conditions that the low-k turbulence spectrum is a mix of low growth rate ITG and TEM instabilities. The ITG modes occupy the entire low-k spectrum near $\rho = 0.5$, but the amount of ITG compared to TEM is a decreasing fraction of the spectrum as radius increases. At large radius the entire spectrum is TEM, with the growth rates increasing linearly with radius for the TEM. Moving forward in time and lower in density in Fig 8(b,e), the growth rates increase for the TEM as the collisionality decreases favoring the TEM, and the region of ITG modes almost completely disappears. At the latest time in Fig. 8(c,f) the ITG modes have completely disappeared and the low-k spectrum is all TEM. The spectral evolution in time and space is a competition between collisions (that decreases everywhere in time) and trapped particle fraction. The ITG modes dominate at low trapped fraction farther into the core, and high collisionality early in time. Later in time the collisionality is significantly reduced, making the TEM dominant. It should be noted that a GYRO simulation at $\rho = 0.5$, $k_\theta \rho_s = 0.5$ can flip the dominant mode from ion to electron direction when ν_{ee} is scaled down to 20% of the experimental value, which points to collisions as a key element causing the transition the dominant mode. Further, in the higher wavenumber range $k_\theta \rho_s > 1$ GYRO indicates unstable ETG modes.

Relating the linear turbulence stability spectrum to the observed plasma rotation profile, we can readily see that *the region in space and in time where the TEM is dominant is associated with a flat main-ion rotation profile.* This result is broadly consistent with the expectations from previous LOC-SOC transition studies and the association between the ITG mode, saturated ohmic confinement, and hollow rotation profiles. However, as is well known, the dominant linear mode is sensitive to the plasma profile gradients and not simply the plasma collisionality, as is the dominant change in this experiment. It is common to explore the linear stability by varying the plasma profiles and gradients within experimental uncertainty for uncertainty quantification[22]. However, an alternate technique is to use parameter scans from turbulence simulations[54] or a transport solver to adjust the profile gradients to match the power flow determined by TRANSP analysis. In the next section, we will use the reduced transport model TGLF inside the transport solver TGYRO to assess our conclusions from this section that the high density conditions are ITG dominated, and the low density conditions are TEM dominant.

V. TRANSPORT MODELING WITH TGYRO AND EIGENVALUE SPECTRUM WITH TGLF

The previous section displayed initial value GYRO simulations that indicate a transition from ITG to TEM turbulence as the plasma density is ramped down in Fig. 3. Rather than performing computationally demanding nonlinear gyrokinetic simulations across the ra-

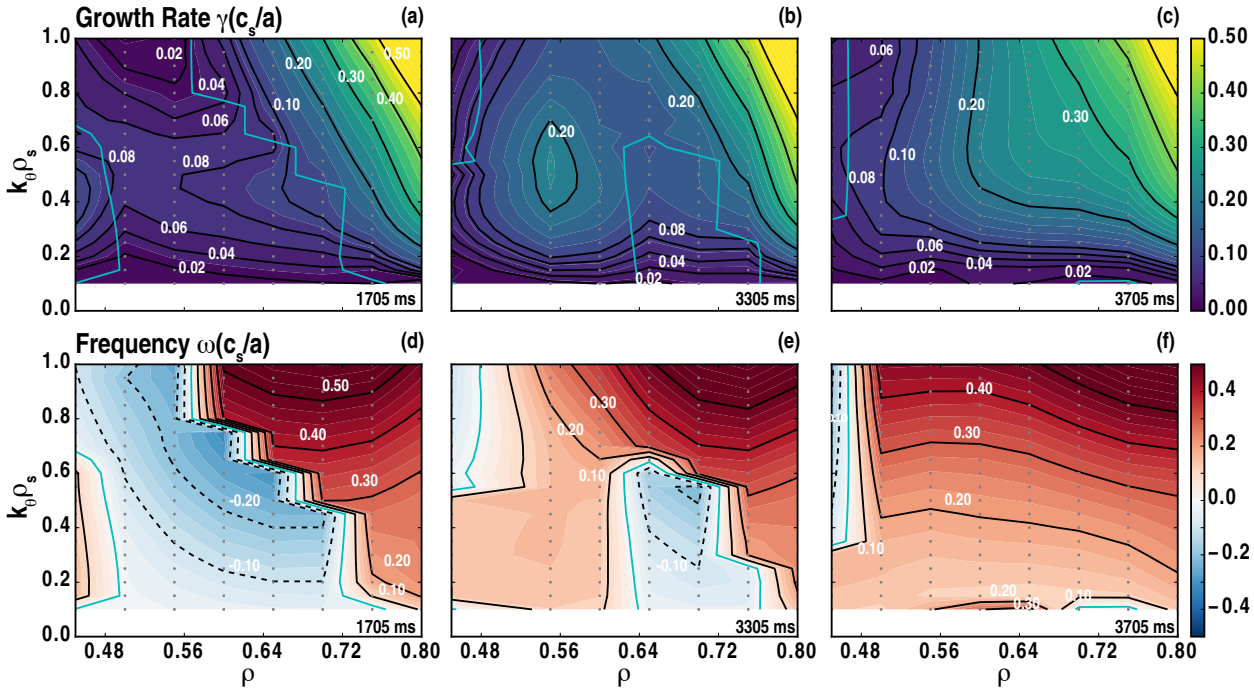

FIG. 8: Evolution of linear turbulence spectrum from three times in Fig. 4 showing the growth rate and frequency of the most unstable mode for highest density with ITG modes (a,d), lowest density before ECH showing mostly TEM (b,e) and lowest density with ECH showing all TEM (c,f). Ion(electron) direction modes are negative(positive) frequency. In all panels the thick cyan line indicates the region of radius and wavenumber where the frequency is zero, denoting the boundary between modes propagating in the ion vs. electron drift direction

dial profile from $\rho = 0.5 - 0.8$ and spanning ITG to ETG scales, we use the trap gyro-Landau fluid (TGLF) model[55, 56] to compute the linear eigenmodes (dominant and first sub-dominant) and quasilinear weights producing gyro-Bohm normalized particle, energy and momentum transport fluxes ($\Gamma/\Gamma_{\rm gB}$, $Q/Q_{\rm gB}$, $\Pi/\Pi_{\rm gB}$). The neoclassical transport, which is relatively small in this case, is computed with NEO[53]. TGLF includes a linear eigenmode spectrum covering ion to electron scales capturing electrostatic ITG, TEM and ETG instabilities. The quasilinear weights in TGLF come from a database of nonlinear GYRO simulations, and therefore are theory-based, but come with a numerical speedup of many orders of magnitude. We use the transport solver TGYRO[57] with the transport flux computed by TGLF and NEO to adjust the profile gradients across a radial domain represented by a number of flux-tubes and produce a profile prediction. In a series of Newton iterations, TGYRO adjusts $a/LT, a/Ln$ and compares the transport flux from TGLF to the power balance transport flux from TRANSP. As the local gradient scale lengths define the profile, at each iteration TGYRO reconstructs the temperature profiles and re-computes the ion-electron energy exchange self-consistently. The solution is converged when the energy flux from TGLF matches the energy flux from TRANSP, and a new set of profile predictions are reported, arriving at the predicted scale lengths and profiles in Fig. 9.

For the same three times during the density rampdown shown as analyzed by GYRO in Fig. 8, we use TGYRO to predict the temperature profiles at 1705 ms in Fig. 9(a,b), 3305 ms in Fig. 9(c,d) and 3705 ms in Fig. 9(e,f). The associated scale lengths that drive the turbulent transport are shown in Fig. 9(g-l) below each profile. Here the profile scale-length figures show filled circles at each radial "flux-tube" in which TGLF is evaluated. In all cases the comparison between the experimental measurements and simulated profiles display good agreement and are well within the experimental uncertainty. In particular, the ion temperature profile is well predicted in all cases, but the central electron temperature is systematically high. This is expected as TGYRO does not include sawtooth mixing inside of the $q = 1$ surface, nor *ad-hoc* enhancement of the thermal transport inside the sawtooth radius. The more stringent test of the model is not the display of the profiles themselves, but more precisely the normalized inverse scale lengths, and regions of over/under predictions of a/L_T can be easily hidden when integrating inwards from the boundary. In each case shown in in Fig. 9(g-l) a/L_T is seen to be monotonically increasing without any gross variation or mis-match in the gradient scale length structure. One important observation is that the final profiles in the radius of interest where the reversal occurs ($\rho \approx 0.6$) faithfully reproduce the experimental variation in collisionality and T_e/T_i, which we believe are important variables in the

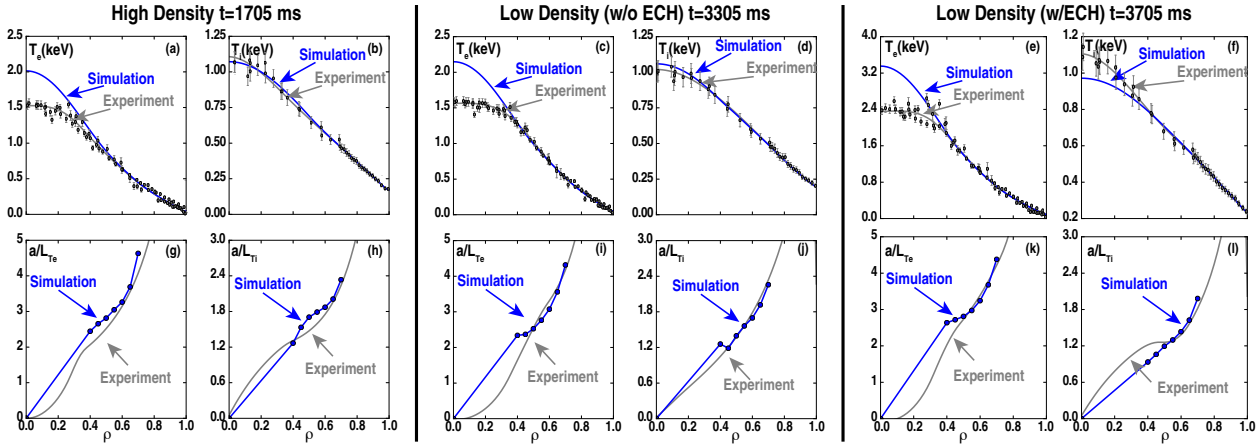

FIG. 9: Radial profiles and normalized inverse scale lengths for three times during density ramp-down. (a,b) Temperatures for high density, (c,d) temperatures for low density before ECH

physics.

Having achieved power-balance flux-matching gradient scale lengths and profiles, we can re-evaluate the linear stability of these profiles to determine if our conclusions from the previous section are consistent. The linear stability maps associated with the simulated profiles shown in Fig. 9 are presented in Fig. 10, and shows similar features as GYRO. First, at high plasma density in Fig. 10(a,d) we show the dominant linear mode and first sub-dominant mode. In Fig. 10(a) TGLF reinforces the conclusion from GYRO that significant ITG activity is present at low-k, and nearly completely covers the range of $k_\theta \rho_s < 1$. However, we also see in Fig. 10(d) that the low-k spectrum possesses both sub-dominant ion and electron modes, including the radial region where the rotation profile hollowing occurs. The lowest plasma density conditions with ohmic heating are shown in Fig. 10(b,e). Here there is some disagreement with the conclusions drawn from the linear GYRO simulations. In Fig. 10(b) the low-k spectrum possesses mostly ion modes, similar to the high density conditions shown in Fig. 10(a), but with a lower groth rate. The sub-dominant modes in Fig. 10(e) are now populated by more electron modes than Fig. 10(d) and with larger growth rates. Comparing the high density and low density ohmic conditions, we concluded that the TGLF flux-matched profiles are dominated by ion modes with sub-dominant electron modes possessing a growth rate that increases as the density drops. These results are consistent with studies on Alcator C-Mod[23], but point to an important conclusion that nearly identical profiles can produce qualitatively different linear mode spectra. At the lowest density with ECH shown in Fig. 10(b,d) we see that TGLF indicates a low-k spectrum almost completely dominated by electron modes in Fig. 10(c). Sub-dominant modes are also in both electron and ion directions, with sub-dominant ion modes in the radial region where the rotation profile hollowing occurs. An important conclusions revealed by these simulations is that the quasilinear TGLF model, covering ion to electron scales, can accurately capture the transport in the higher density conditions with ITG instabilities and the low density case with high T_e/T_i dominated by TEM instabilities, consistent with previous validation using GYRO[54].

From the GYRO simulations of experimental profiles and dominant TGLF eigenmodes from flux-matched profiles, we can conclude that the two states of hollow main-ion rotation and flat main-ion rotation are occurring in a transition region between ITG and TEM regimes for the dominant eigenmodes, respectively. However, as it has been indicated in the past from database studies of ASDEX-Upgrade[25], when a broad survey is performed there is a tendency to conclude that the turbulence is in a "mixed mode" condition, marginal to both ITG and TEM. The study here using GYRO and TGLF illustrates the pitfalls of a binary classification of the plasma conditions being either ITG or TEM, particularly if no uncertainty quantification or power balance flux-matching is performed. Indeed the dominant mode varies with radius, and there are sub-dominant modes that also play a role in the transport.

While we have shown previously in this article that gyrokinetic and gyrofluid modeling of the linear instabilities and thermal transport allows us to make conclusions about the modes that drive transport and the level of heat flux produced, local gyrokinetic and quasilinear modeling does not contain many of the mechanisms needed to describe the symmetry breaking that produce the residual stresses required to explain intrinsic rotation profiles. In a flux tube simulation with an up/down symmetric equilibrium and no rotation or shear, the momentum flux has been proven to be identically zero. Therefore, in a situation where the experimental momentum flux is zero (as in intrinsic torque-free conditions), any attempt to simulate the momentum transport by flux-matching will produce the trivial solution of nearly zero rotation gradient. This is because the mechanisms in the model capable of generating the zero flux state are lim-

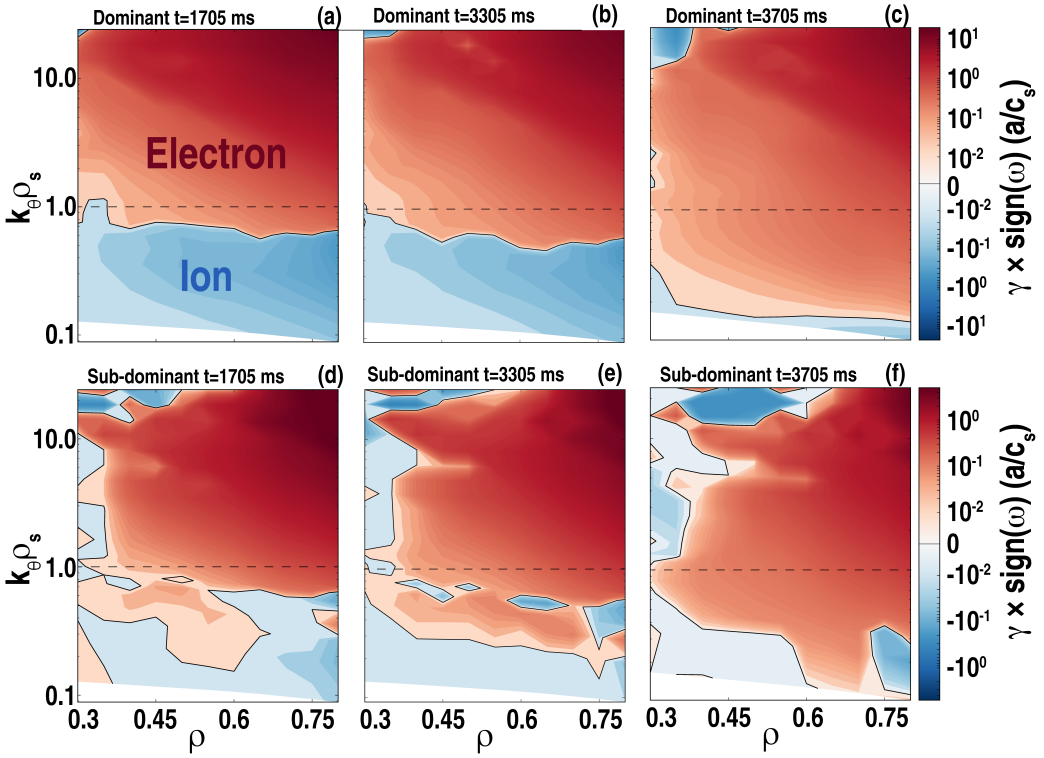

FIG. 10: TGLF dominant (a,b) and sub-dominant (c,d) eigenvalue frequency and growth rates corresponding to TGYRO flux-matched simulations in Fig. 9 at high density time t=1705 ms(a,d), low density without ECH t=3305 ms(b,e) and low density with ECH t=3705 ms(c,f)

ited to the momentum diffusion $-\chi_\varphi \partial\Omega/\partial r$ and the (relatively small) pinch $V_p\Omega$, shown in Eq. 1. Hence $\Pi = 0$ is trivially well satisfied by $\partial\Omega/\partial r = 0$. However, as we observe, $\partial\Omega/\partial r$ is clearly non-zero, and can produce a significant diffusive momentum flux that must be counteracted by Π_{resid} to produce the zero flux state.

To illustrate these qualitative statements with quantitative modeling, we perform a simulation using TGLF including the momentum pinch and self-consistently vary the rotation gradient and $\mathbf{E}\times\mathbf{B}$ shear from Fig. 4(a) at $\rho = 0.6$ starting from zero and scan up to four times the experimental value, shown in Fig. 11. Here the parameter α is a multiplier on the experimental rotation shear and $\mathbf{E}\times\mathbf{B}$ shear, where a value of $\alpha = 1.0$ is the experimental value. The variation of the particle flux Fig. 11(a) and energy flux Fig. 11(b) display the expected trends that increasing the $\mathbf{E}\times\mathbf{B}$ shear weakly reduces the transport up to the experimental value of $\alpha = 1.0$, and then more strongly suppress the radial flux of particles and energy at twice the experimental value of α and above. The particle flux also transitions from outward to inward as the ITG modes are suppressed, which would result in density peaking. The momentum transport shown in Fig. 11(c) is qualitatively different. Clearly, at $\alpha = 0.0$ there is little momentum transport $\Pi \approx 0$ and the momentum transport at this value is due to a small momentum pinch pulling positive angular momentum from the edge into the core. The pinch would act to peak the rotation, because a negative momentum flux from the pinch would require a positive diffusive flux to reach a zero flux state. As the rotation and $\mathbf{E}\times\mathbf{B}$ shear is increased to the experimental value $\alpha = 1.0$, the momentum flux increases linearly in the negative direction because the positive rotation gradient drives inward diffusion and the $\mathbf{E}\times\mathbf{B}$ shear is too small to reduce the turbulent transport. At the experimental value of $\alpha = 1.0$, TGLF indicates that the rotation gradient is producing order unity gyro-Bohm level of momentum flux ($\Pi/\Pi_{\rm gB} \approx 1.5$). To put this momentum flux into context, $\Pi/\Pi_{\rm gB} \approx 1.5$ at mid-radius corresponds to 8×10^{-3} Nm/m^2. This level of momentum flux across mid-radius corresponds to approximately one fourth of an 81 kV DIII-D tangential neutral beam operating at 2 MW in L-mode (low density) conditions. As α increases above the experimental level, the slope of the momentum flux transitions and rolls over because now the $\mathbf{E}\times\mathbf{B}$ shear has reached a level that begins to suppress turbulent transport. In principle, there is a second condition where $\Pi \approx 0$ at high rotational shear where the turbulence is quenched (ion neoclassical), but in practice this condition would be difficult to access without the use of neutral beam injection as an acuator. There is evidence of DIII-D discharges operating on both slopes of this momentum flux curve[58, 59], where the incremental momentum diffusivity $\partial\Pi/\partial\gamma_p$ is negative, but at finite torque and regimes dominated by turbulent transport.

Mechanisms that produce positive momentum flux in

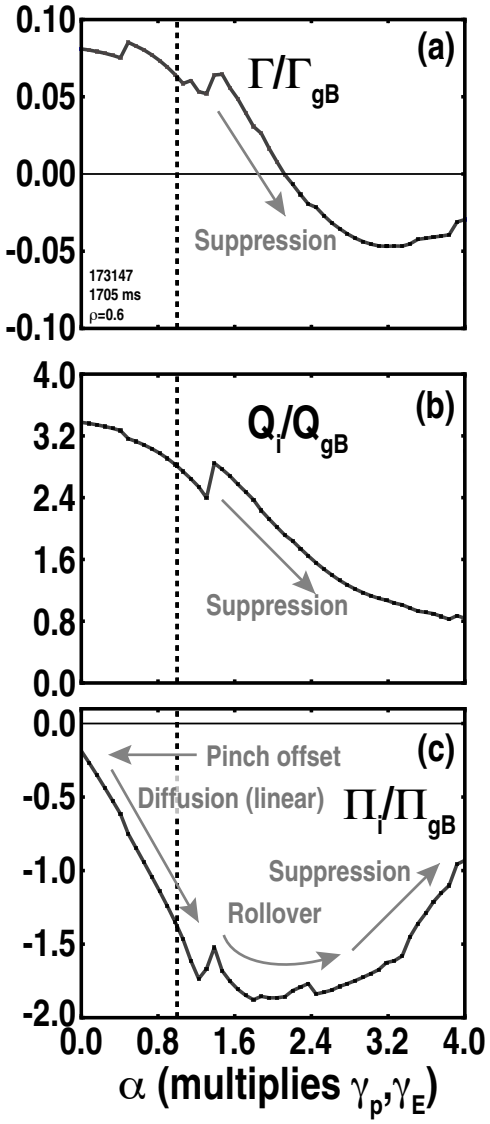

FIG. 11: Illustration of particle, energy and momentum flux with self-consistent rotation shear γ_p and $\mathbf{E}\times\mathbf{B}$ shear γ_E scaled by factor α across the range from zero to four times the experimental level. Vertical dashed line at experimental level ($\alpha = 1$). (a) Particle flux reduces and changes sign from outward to inward, (b) thermal energy transport reduces and (c) momentum flux initially becomes more negative reaching more than unity $\Pi/\Pi_{\rm gB}$ and then rolls over due to $\mathbf{E}\times\mathbf{B}$ shear suppression.

absence of a rotation gradient via symmetry breaking are clearly needed to achieve the profile seen in Fig. 4(a) and balance against the approximately unity gyro-Bohm level of inward momentum diffusion. In the next section, we will use a global gyrokinetic simulation to investigate such mechanisms that produce a positive offset in Fig. 11(c) and show that the hollow rotation profile is due to a wide region of positive residual stress momentum flux, whereas the flat profile is due to finite stress that lacks large-scale structure.

VI. GLOBAL NONLINEAR GYROKINETICS WITH GTS

The previous sections Sec. IV, V have shown that in the high density and low density conditions with ECH there is a predominance of ITG and TEM turbulent instabilities, respectively. To address mechanisms that break the toroidal symmetry and produce residual stress momentum flux we use the gradient driven δf particle-in-cell approach with GTS[60] for a qualitative assessment of the stress structure and balance between stress and diffusion. Detailed comparisons of the transport produced by these global simulations is the subject of future investigation. GTS simulations are nonlinear and global, include mechanisms such as equilibrium and profile curvature and turbulence intensity gradients in an up/down asymmetric equilibrium. It is noteworthy that radially global GYRO has also been used to investigate the residual stress in DIII-D discharges[61] and shown experimentally relevant levels of residual stress, and GKW has shown good agreement with intrinsic rotation profiles on ASDEX-Upgrade [48].

GTS simulations have been used recently to investigate DIII-D plasmas for a scan in ECH power[43, 62], and is used here in a similar way. These simulations use kinetic electrons and main-ions, electron and ion collisions. The impurity carbon is not treated as a kinetic species in these simulations, as quasilinear estimates indicate that carbon is a sub-dominant contributor to the momentum flux in these conditions. Plasma profiles including the force balance electric field are read from experimental TRANSP analysis used previously in this paper. The spatial grid size in the perpendicular direction is approximately equal to or less than the local ion gyroradius ρ_i, and a large number of simulation particles (80 per cell per species) is used in order to achieve good statistics. Simulations cover the wavenumber range from $k_\perp\rho_i \leq 2$, which includes the low-k turbulence due to ITG and TEMs. These nonlinear GTS simulations have been performed in a radial domain from $r/a = 0.02-0.95$ using the up/down asymmetric equilibrium shape, q profile and experimental plasma profiles $(n_e, T_e, T_i, Z_{\rm eff})$ as inputs and simulated the turbulence and total momentum transport. The profiles that are simulated are those that produce the linear GYRO spectrum in Fig. 8, and have not been taken from the TGLF flux-matched profiles show previously in this article. Each simulation is run through the initial linear phase and transport overshoot, achieving a quasi-steady turbulent state for time-averaging. Three conditions have been simulated corresponding to the high density ohmic conditions shown in Fig. 4(a), low density ohmic conditions shown in Fig. 4(e) and low density conditions with ECH shown in Fig. 4(f).

When GTS is executed with the rotation profile set to zero everywhere ($\Omega \equiv 0$), then the total momentum flux produced in the simulation is attributed to the residual stress ($\Pi = \Pi_{\rm resid.}$). The result of the zero rotation simulations are shown in Fig. 12, where the residual stress

from the simulation is defined in Ref. [62]. In Fig. 12(a) for the high density ITG dominated case, we see that near $\rho \approx 0.6$ that there is a broad, positive region of residual stress. The existence of this positive residual stress will act to produce a positive rotation gradient, i.e. a hollow profile. In this case dominated by linearly unstable ITG modes, the residual stress most strongly correlates with the shearing rate produced by zonal flows[63, 64] $\gamma^{ZF}_{E\times B}$, which is the shear in the zonal flow electric field. As the density is lowered but the heating remains ohmic, the simulation is quite different. The zonal flow shearing in Fig. 12(b) remains the symmetry breaking mechanism that correlates with the residual stress, but the structure of the stress has changed. There are radial oscillations in the residual stress, but the profile lacks any large-scale "dipole-like" broad stress structure. At low collisionality dominated by linearly unstable TEMs in Fig. 12(c), there are radial oscillations in the residual stress similar to Fig. 12(b), but now most strongly correlates with the turbulence intensity gradient. Here at low density, the residual stress most strongly correlates with the turbulence intensity gradient[65] for symmetry breaking $d\langle\delta\Phi^2\rangle/d\rho$. The oscillatory nature and relatively low magnitude of the stress in Fig. 12(b,c) will produce a rotation profile that is relatively flat compared to Fig. 12(a).

In the same fashion as Ref. [43, 48], we can produce a prediction of the main-ion toroidal rotation by using the residual stresses in Fig. 12(a-c) balanced against turbulent momentum diffusion. The resulting rotation profile formed by integrating the momentum balance equation neglecting the small pinch is shown in Fig. 13. Here we can see the quantitative realization of the qualitative expectations that the broader "dipole-like" residual stress produces a rotation profile hollowing at mid-radius, whereas the oscillatory residual stress creates and oscillating rotation profile prediction, without broad peaking or hollowing. Returning to the description of the observations as presented in Sec. III, we postulated that the hollow profile must be due to a locally positive residual stress but the flat profile could be formed by diffusion alone. We see from the GTS simulations that indeed a positive residual stress in the hollow rotation case is predicted by the gyrokinetic simulations. But rather than utterly lacking residual stress in the low density plasma with ECH, we see that there is finite residual stress that oscillates across the radial profile.

Given the ability of GTS (and GKW in Ref. [48]) to produce the qualitative features of the residual stress needed to describe the momentum transport, and the reasonable quantitative agreement predicting the rotation profile, the obvious next question is whether the physics of the residual stress can be distilled into a simplified quasilinear description. Such a capability to capture the essential physics of symmetry breaking and magnitude of the residual stress in a reduced model would open the door to integrated simulations of intrinsic rotation conditions and low-torque scenarios. Progress has already been made in a quasilinear description of symmetry breaking by the tilt of the eigenmode[66], but more work is required to validate the numerous symmetry breaking mechanisms and capture the variety of intrinsic rotation phenomena. In the next section, we will show progress in the ability to capture the energy confinement and evolution of the dominant instabilities, which when combined with a model for the residual stress will permit predictions of low torque scenarios for assessment of stability and confinement.

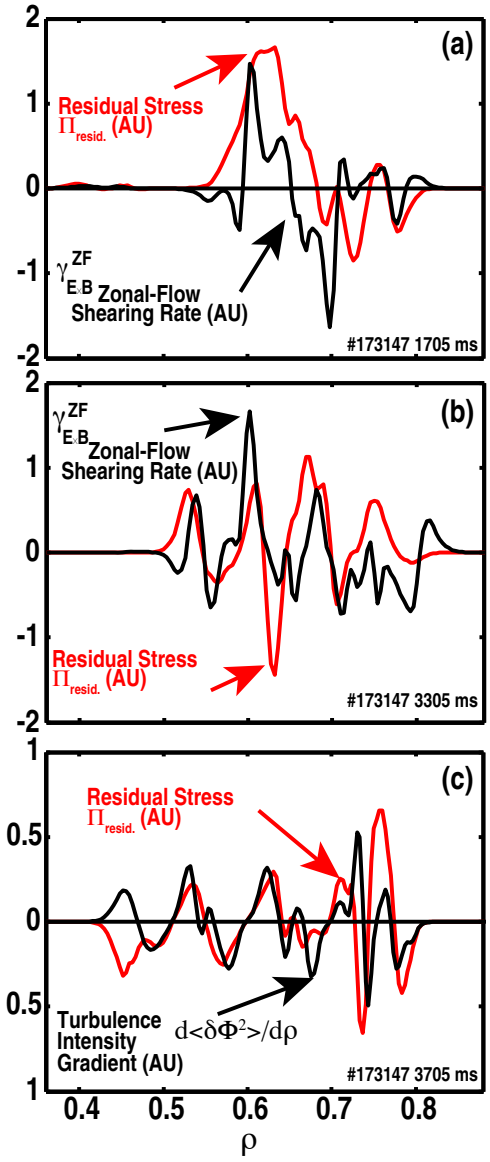

FIG. 12: Radial profiles of residual stress and symmetry breaking mechanism for (a) high density ohmic (b) low density ohmic, and (c) low density with ECH. Arbitrary units are used to show the spatial correlation between turbulence and residual stress structure.

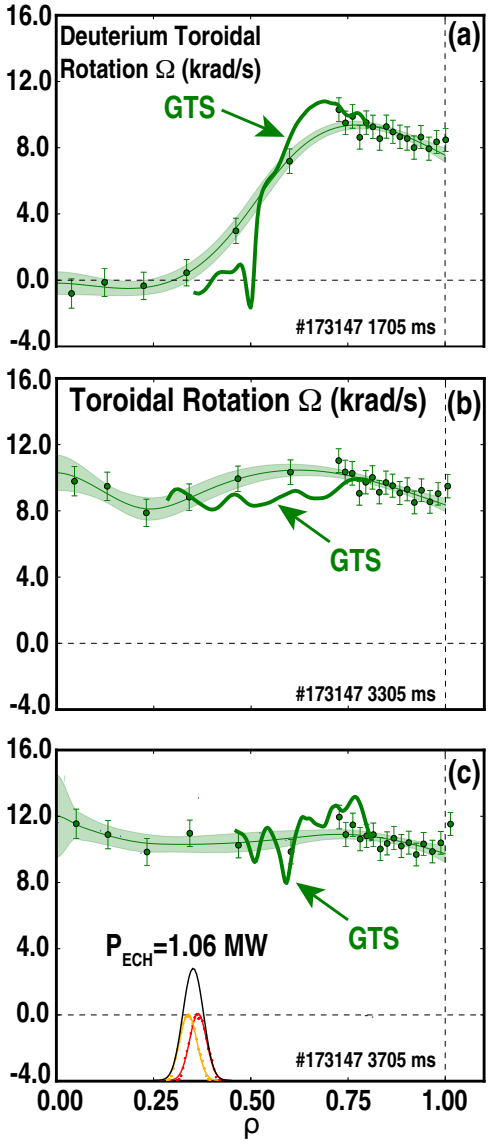

FIG. 13: Profiles of main-ion toroidal rotation formed by balancing the residual stress profiles in Fig. 12 against momentum diffusion. (a) High density ohmic, (b) low density ohmic, and (c) low density with ECH.

VII. TIME DEPENDENT PREDICTIVE TRANSPORT MODELING WITH TRANSP

In the previous sections we have investigated a slow density ramp-down with "snapshot" analysis at key times, demonstrating the transition from conditions dominated by ITG modes to conditions dominated by TEMs as the collisionality is reduced. We have seen that the change in the linear mode character guides the expectation of ITG modes producing hollow rotation profiles, and TEMs producing flat rotation profiles. When combined with a reduced model for the symmetry breaking mechanisms and residual stress momentum flux, it is possible that time-dependent, integrated simulations of the rotation profile expected in low-torque scenarios can be achieved. To that end, we now revisit the "classic" method of achieving a clear LOC-SOC transition first shown in Fig. 2. For this LOC-SOC density ramp-up experiment, we use time dependent predictive TRANSP simulations with TGLF. This TRANSP capability has already been used to explain the phenomena of cold pulse temperature inversions [67] on Alcator C-Mod, and recently it has been shown that TGLF in the ASTRA modeling was able to reproduce the relevant features of the LOC-SOC transition in ASDEX-Upgrade[21].

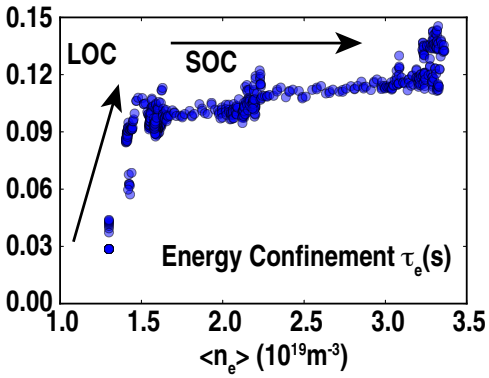

FIG. 14: Energy confinement transition from LOC to SOC from time dependent predictive TRANSP simulation using TGLF.

Predictive TRANSP has been used here to test the ability of TGLF to capture the energy confinement saturation, and examine the linear mode spectrum associated with any confinement changes. Here, we use the experimental equilibrium flux surfaces and evolve the current resistively in time. We allow the temperatures and density to be predicted by TGLF inside $\rho = 0.8$, with the radiated power used from the experimental bolometry. The experimental impurity density is used during the times of the neutral beam blips and linearly interpolated connecting the sparse measurements. The only heating in the simulation is ohmic, as the power delivered by the neutral beam blips was omitted in the predictive simulation. Shown in Fig. 14 is the energy confinement time as a function of the volume averaged electron density. Similar to Fig. 2(a), we see that the energy confinement transitions from linearly increasing with density, to nearly saturated with density above a critical density. It can be seen that the transition in Fig. 14 near $\langle n_e \rangle \approx 1.5 \times 10^{19}$ m^{-3} occurs at a slightly lower density than the experimental Fig. 2(a), $\langle n_e \rangle \approx 1.7 \times 10^{19}$ m^{-3}, and that the confinement saturation is not completely independent of density. Nevertheless, we can use this simulation to investigate the landscape of turbulent instabilities and how they evolve in time.

Execution of TGLF in TRANSP provides the eigenvalue spectrum as a standard output for inspection in space in time[46]. The growth rate γ and frequency ω are three dimensional objects in $(\rho, t, k_\theta \rho_s)$ that can be

indexed for visualization, with a particularly informative representation of $\gamma(k_\theta \rho_s)$ taken for a fixed radial position and colored by time, shown in Fig. 15. The landscape of unstable eigenmodes viewed in a log-log representation presents a number of interesting features relevant to the thermal transport. First, the growth rates and frequencies in Fig. 15(a,b)indicate that early in time the spectrum has a growth rate that is a monotonically increasing function of wavenumber with modes in the electron direction ($\omega > 0$). Here at early time the spectrum is dominated by TEMs in the low-k and ETG in the high-k. As time evolves, the growth rate spectrum develops into a double-peak separating the low-k and high-k regions with reduced growth rate in the TEM range ($k_\theta \rho_s \approx 1.0$). In the frequency spectrum, we see a progressive evolution of low-k modes flipping from the electron to ion direction as time evolves and the density rises. These calculations show that the unstable eigenmodes smoothly transition from a TEM/ETG condition, to an ITG/ETG condition.

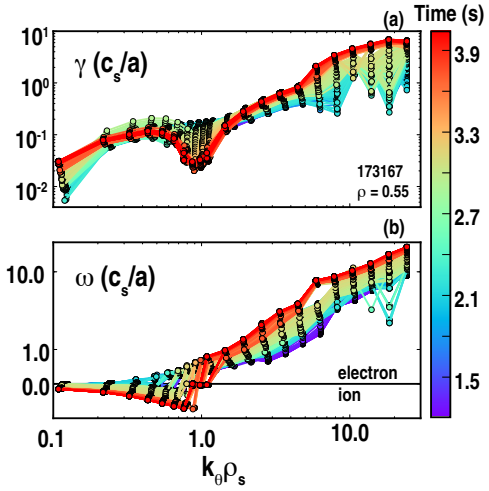

FIG. 15: Linear turbulence spectrum from TGLF spanning ion to electron scales as time evolves and density increases. (a) Linear growth rate γ and (b) frequency ω show transition from TEM/ETG to ITG/ETG as time and density increase.

Looking more closely at the low-k, a spectrum on a linear-linear scale has been produced to view the instability progression. In Fig. 16(a) the decrease of the TEM growth rate in time near $k_\theta \rho_s \approx 1.0$ and separation into ITG/ETG at late time is evident, as the frequency of the modes in Fig. 16(b) progressively flip from positive to negative. One noticeable feature Fig. 16(a) is a transient burst of low-k ion direction modes near 3.0 s, and this is caused by a step up in plasma density and drop in $Z_{\rm eff}$ that increases the ion energy flux driving ITG modes. This occurs as the plasma density in Fig. 14 is increased from $\langle n_e \rangle = 2.2 \rightarrow 3.0$. These transient phenomena show a more complex picture than can be captured by well chosen timeslice analysis, and highlight the ability of time-dependent simulations to capture dynamic events such as perturbative heat pulses that change the plasma linear stability. As parameterizations of turbulent residual stresses are developed in the future, predictive TRANSP simulations with TGLF and other reduced transport models will serve as a convenient platform for validation.

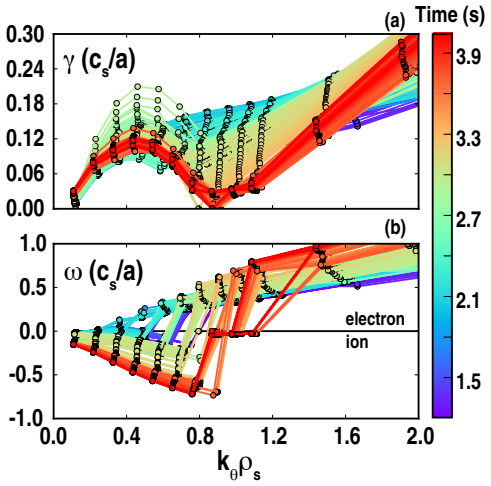

FIG. 16: Low-k linear turbulence spectrum from Fig. 15 on a linear-linear scale as time evolves and density increases. (a) Linear growth rate γ and (b) frequency ω show transition from low-k TEM to ITG as time and density increase.

VIII. DISCUSSION AND CONCLUSIONS

In this article we have shown that direct measurements of the main-ion intrinsic toroidal rotation can provide insight into both the shape and magnitude of the turbulent residual stress: i.e. the local momentum flux required to balance against turbulent momentum diffusion in stationary torque-free conditions. It is the gradient of the rotation profile that reveals the shape and magnitude of the underlying residual stress, and we have shown that the main-ion and impurity rotation profiles can possess even qualitatively different gradients. This fact bears directly on the search for theoretical mechanisms that capture observed intrinsic rotation profiles, as rotation profile gradients from impurity measurements may be misleading. Expectations of the main-ion rotation profile can be reasonably well captured in these ohmic plasmas by computing the neoclassical poloidal flow in the radial force balance, but not in all conditions, highlighting the need for direct main-ion rotation measurements.

In the well-known LOC-SOC transition, these DIII-D experiments and simulations add to a body of knowledge on the turbulent transport physics associated with a transition in thermal energy confinement, with the hallmark rotation reversal. By executing a slow density ramp-down experiment and performing gyrokinetic simulations at key times, we show that the turbulent stability evolves subtly in both space and wavenumber. From GYRO, the transition from LOC to SOC occurs

as TEMs are collisional stabilized and replaced by ITGs from the outer radii inwards, occupying an increasing fraction of the low-k spectrum as the density is increased. In these Ohmic conditions on DIII-D, a binary classification would state that the flat rotation is associated with dominantly linearly unstable TEMs and the hollow rotation associated with dominantly linearly unstable ITGs. Gyrofluid modeling using TGLF with power-balance flux-matching through TGYRO reveals that the experimental profiles are in good theoretical power balance, and supports the conclusions from linear GYRO. However, TGLF indicates that a binary classification of ITG vs. TEM is too crude, as the ITG conditions have sub-dominant TEMs and vice-versa. It is worth noting that advances in integrated modeling[44] have made these previously tedious exercises expedient, providing a more comprehensive evaluation of the transport in radius, time and wavenumber.

In plasma scenarios with little external angular momentum injection, understanding and being able to predict the shape and magnitude of the turbulent residual stress remains a key challenge. Global gyrokinetic simulations in this paper and elsewhere have shown that residual stresses of the correct sign and magnitude to explain the observations can be generated in ohmic plasma conditions. These unique simulations should used to gain insight into the symmetry breaking mechanisms and how they scale (i.e. with normalized gyroradius) to ITER and future reactors. We note that an *ab initio* predictive capability for future experiments has yet to be demonstrated. Upon achievement of such reduced models of residual stress generation, predictive TRANSP simulations with TGLF offer a vehicle for assessing plasma performance and stability in the face of self-generated rotation.

IX. ACKNOWLEDGEMENTS

This material is based upon work supported by the U.S. Department of Energy, Office of Science, Office of Fusion Energy Sciences, using the DIII-D National Fusion Facility, a DOE Office of Science user facility, under Awards DE-AC02-09CH11466, DE-FC02-04ER54698, DE-FG02-08ER54999, DE-FG02-07ER54917, DE-FG03-97ER54415, DE-FG02-04ER54235 and DE-FG02-08ER54984. DIII-D data shown in this paper can be obtained in digital format by following the links at https://fusion.gat.com/global/D3D_DMP. Part of the data analysis was performed using the OMFIT integrated modeling framework [44]. GTS simulations were performed on Edison at NERSC. B. A. Grierson acknowledges valuable discussions with K.H. Burrell, W.M. Solomon, J.S. deGrassie, J.A. Boedo, T. Stoltzfus-Dueck, A. Bortolon, G.M. Staebler, J. Candy, E. Belli, S.P. Smith, O. Meneghini, D. Ernst, W. Hornsby, C. Angioni and R. Nazikian

[1] R. Moyer, C. Paz-Soldan, R. Nazikian, D. Orlov, N. Ferraro, B. Grierson, M. Knölker, B. Lyons, G. McKee, T. Osborne, et al., Phys. Plasmas **24** (2017), ISSN 10897674.

[2] R. Nazikian, C. Paz-Soldan, J. Callen, J. Degrassie, D. Eldon, T. Evans, N. Ferraro, B. Grierson, R. Groebner, S. Haskey, et al., Phys. Rev. Lett. **114** (2015), ISSN 10797114.

[3] B. Tobias, M. Chen, I. G. J. Classen, C. W. Domier, R. Fitzpatrick, B. A. Grierson, N. C. Luhmann, C. M. Muscatello, M. Okabayashi, K. E. J. Olofsson, et al., Phys. Plasmas **23**, 056107 (2016), ISSN 1070-664X, URL http://aip.scitation.org/doi/10.1063/1.4946026.

[4] K. H. Burrell, Phys. Plasmas **4**, 1499 (1997).

[5] C. L. Fiore, D. R. Ernst, Y. A. Podplay, D. Mikkelsen, and N. T. Howard, Phys. Plasmas **19**, 56113 (2012), URL http://pop.aip.org/resource/1/phpaen/v19/i5/p056113{_}s1.

[6] J. L. Luxon, Nucl. Fusion **42**, 614 (2002).

[7] Y. Camenen, C. Angioni, A. Bortolon, B. P. Duval, E. Fable, W. A. Hornsby, R. M. McDermott, D. H. Na, Y. S. Na, A. G. Peeters, et al., Plasma Phys. Control. Fusion **59**, 34001 (2017), URL http://iopscience.iop.org/article/10.1088/1361-6587/aa543a.

[8] J. E. Rice, J. Phys. Conf. Ser. **123**, 012003 (2008), ISSN 1742-6596, URL http://stacks.iop.org/1742-6596/123/i=1/a=012003?key=crossref.43e00a209bb63a52f7ce442c76d3b21b.

[9] J. S. DeGrassie, Plasma Phys. Control. Fusion **51**, 124047 (2009).

[10] P. H. Diamond, Y. Kosuga, Ö. D. Gürcan, C. J. McDevitt, T. S. Hahm, N. Fedorczak, J. E. Rice, W. X. Wang, S. Ku, J. M. Kwon, et al., Nucl. Fusion **53**, 104019 (2013), URL http://stacks.iop.org/0029-5515/53/i=10/a=104019?key=crossref.0c42bf3e71c984abf92f8d264489ab28.

[11] K. Ida and J. E. Rice, Nucl. Fusion **54**, 45001 (2014), URL http://stacks.iop.org/0029-5515/54/i=4/a=045001?key=crossref.b8c8c6e201805bfdef142a1ccc5ca6c7.

[12] J. S. DeGrassie, J. E. Rice, K. H. Burrell, R. J. Groebner, and W. M. Solomon, Phys. Plasmas **14**, 56115 (2007).

[13] B. Grierson, K. Burrell, W. Solomon, and N. Pablant, Rev. Sci. Instrum. **81** (2010), ISSN 00346748.

[14] B. Grierson, K. Burrell, C. Chrystal, R. Groebner, D. Kaplan, W. Heidbrink, J. Muñoz Burgos, N. Pablant, W. Solomon, and M. Van Zeeland, Rev. Sci. Instrum. **83** (2012), ISSN 00346748.

[15] B. Grierson, K. Burrell, W. Heidbrink, M. Lanctot, N. Pablant, and W. Solomon, Phys. Plasmas **19** (2012), ISSN 1070664X.

[16] B. Grierson, K. Burrell, C. Chrystal, R. Groebner, S. Haskey, and D. Kaplan, Rev. Sci. Instrum. **87** (2016), ISSN 10897623.

[17] S. Haskey, B. Grierson, K. Burrell, C. Chrystal, R. Groebner, D. Kaplan, N. Pablant, and L. Stagner, Rev. Sci. Instrum. **87** (2016), ISSN 10897623.

[18] S. R. Haskey, B. A. Grierson, L. Stagner, C. Chrystal, A. Ashourvan, A. Bortolon, M. D. Boyer, K. H. Burrell, C. Collins, R. J. Groebner, et al., Rev. Sci. Instrum. **89**, 10D110 (2018), ISSN 0034-6748, URL http://aip.scitation.org/doi/10.1063/1.5038349.

[19] R. Parker, M. Greenwald, S. Luckhardt, E. Marmar, M. Porkolab, and S. Wolfe, Nucl. Fusion **25**, 1127 (1985), ISSN 0029-5515, URL http://stacks.iop.org/0029-5515/25/i=9/a=023?key=crossref.9a6c3f4ecf191fcd07bb61632c817206.

[20] J. Rice, C. Gao, M. Reinke, P. Diamond, N. Howard, H. Sun, I. Cziegler, A. Hubbard, Y. Podpaly, W. Rowan, et al., Nucl. Fusion **53**, 033004 (2013), ISSN 0029-5515, URL http://iopscience.iop.org/0029-5515/53/3/033004/article/http://stacks.iop.org/0029-5515/53/i=3/a=033004?key=crossref.55edc17c8ecfad516c4dc14840578750.

[21] I. Erofeev, E. Fable, C. Angioni, and R. McDermott, Nucl. Fusion **57**, 126067 (2017), ISSN 0029-5515, URL http://iopscience.iop.org/article/10.1088/1741-4326/aa8e32http://stacks.iop.org/0029-5515/57/i=12/a=126067?key=crossref.2fd71eca4b23c782775535e304a9be75.

[22] C. Holland, Phys. Plasmas **23**, 60901 (2016), URL http://scitation.aip.org/content/aip/journal/pop/23/6/10.1063/1.4954151.

[23] N. T. Howard, A. E. White, M. Greenwald, C. Holland, J. Candy, and J. E. Rice, Plasma Phys. Control. Fusion **56**, 124004 (2014), URL http://stacks.iop.org/0741-3335/56/i=12/a=124004?key=crossref.66d7139b1428ea2448f900b3295a1a05.

[24] P. Ennever, M. Porkolab, J. Candy, G. M. Staebler, M. L. Reinke, J. E. Rice, J. C. Rost, D. R. Ernst, C. Fiore, J. W. Hughes, et al., Phys. Plasmas **22**, 72507 (2015), URL http://scitation.aip.org/content/aip/journal/pop/22/7/10.1063/1.4926518.

[25] C. Angioni, R. M. McDermott, F. Casson, E. Fable, A. Bottino, R. Dux, R. Fischer, Y. Podoba, T. Putterich, F. Ryter, et al., Phys. Rev. Lett. **107**, 215003 (2011), URL http://prl.aps.org/abstract/PRL/v107/i21/e215003.

[26] R. M. McDermott, C. Angioni, G. D. Conway, R. Dux, E. Fable, R. Fischer, T. Putterich, F. Ryter, E. Viezzer, and t. A. U. Team, Nucl. Fusion **54**, 43009 (2014), URL http://stacks.iop.org/0029-5515/54/i=4/a=043009?key=crossref.04ef6f6c7e1445fb03f9a663effdf8b7.

[27] R. J. Hawryluk, Course Phys. Plasmas Close to Thermonucl. Cond. pp. 1–28 (1979).

[28] R. J. Goldston, D. C. McCune, H. H. Towner, S. L. Davis, R. J. Hawryluk, and G. L. Schmidt, J. Comput. Phys. **43**, 61 (1981).

[29] F. Poli, J. Sachdev, J. Breslau, M. Gorelenkova, and X. Yuan, *Transp v18.2*, [Computer Software] https://dx.doi.org/10.11578/dc.20180627.4 (2018), URL https://dx.doi.org/10.11578/dc.20180627.4.

[30] A. Pankin, D. McCune, R. Andre, G. Bateman, and A. H. Kritz, Comput. Phys. Commun. **159**, 157 (2004).

[31] J. E. Rice, M. J. Greenwald, Y. A. Podpaly, M. L. Reinke, P. H. Diamond, J. W. Hughes, N. T. Howard, Y. Ma, I. Cziegler, B. P. Duval, et al., Phys. Plasmas **19**, 056106 (2012), ISSN 1070-664X, URL http://pop.aip.org/resource/1/phpaen/v19/i5/p056106{_}s1http://aip.scitation.org/doi/10.1063/1.3695213.

[32] J. C. Hillesheim, F. I. Parra, M. Barnes, N. A. Crocker, H. Meyer, W. A. Peebles, R. Scannell, A. Thornton,

and t. M. Team, Nucl. Fusion **55**, 32003 (2015), URL http://stacks.iop.org/0029-5515/55/i=3/a=032003?key=crossref.5d8898a9db7caab7b45d6b63e116d164.

[33] J. S. DeGrassie, S. H. Müller, and J. A. Boedo, Nucl. Fusion **52**, 13010 (2012), URL http://iopscience.iop.org/0029-5515/52/1/013010.

[34] J. A. Boedo, E. A. Belli, E. M. Hollmann, W. M. Solomon, D. L. Rudakov, and K. H. Burrell, Phys. Plasmas **18** (2011), URL http://link.aip.org/link/?PHPAEN/18/032510/1.

[35] T. Stoltzfus-Dueck, Phys. Rev. Lett. **108**, 65002 (2012), URL http://prl.aps.org/abstract/PRL/v108/i6/e065002.

[36] J. Boedo, J. DeGrassie, B. Grierson, T. Stoltzfus-Dueck, D. Battaglia, D. Rudakov, E. Belli, R. Groebner, E. Hollmann, C. Lasnier, et al., Phys. Plasmas **23** (2016), ISSN 10897674.

[37] A. Ashourvan, B. A. Grierson, D. J. Battaglia, S. R. Haskey, and T. Stoltzfus-Dueck, Phys. Plasmas **25**, 056114 (2018), ISSN 1070-664X, URL http://aip.scitation.org/doi/10.1063/1.5018326.

[38] A. G. Peeters, C. Angioni, and D. Strintzi, Phys. Rev. Lett. **98**, 27 (2007), ISSN 00319007.

[39] T. S. Hahm, P. H. Diamond, Ö. D. Gürcan, and G. Rewoldt, Phys. Plasmas **14**, 72302 (2007), URL http://scitation.aip.org/getabs/servlet/GetabsServlet?prog=normal{&}id=PHPAEN000014000007072302000001{&}idtype=cvips{&}gifs=yes.

[40] W. M. Solomon, K. H. Burrell, A. M. Garofalo, A. J. Cole, R. V. Budny, J. S. DeGrassie, W. W. Heidbrink, G. L. Jackson, M. J. Lanctot, R. Nazikian, et al., Nucl. Fusion **49**, 85005 (2009), URL http://iopscience.iop.org/article/10.1088/0029-5515/49/8/085005.

[41] J. S. DeGrassie, K. H. Burrell, L. R. Baylor, W. Houlberg, and J. Lohr, Phys. Plasmas **11**, 4323 (2004), ISSN 1070-664X, URL http://aip.scitation.org/doi/10.1063/1.1778751.

[42] Y. J. Shi, W. H. Ko, J. M. Kwon, P. H. Diamond, S. G. Lee, S. H. Ko, L. Wang, S. Yi, K. Ida, L. Terzolo, et al., Nucl. Fusion **53**, 113031 (2013), URL http://iopscience.iop.org/article/10.1088/0029-5515/53/11/113031.

[43] B. Grierson, W. Wang, S. Ethier, G. Staebler, D. Battaglia, J. Boedo, J. S. DeGrassie, and W. Solomon, Phys. Rev. Lett. **118**, 015002 (2017), ISSN 0031-9007, URL https://link.aps.org/doi/10.1103/PhysRevLett.118.015002.

[44] O. Meneghini, S. Smith, L. Lao, O. Izacard, Q. Ren, J. Park, J. Candy, Z. Wang, C. Luna, V. Izzo, et al., Nucl. Fusion **55**, 083008 (2015), ISSN 0029-5515, URL http://stacks.iop.org/0029-5515/55/i=8/a=083008?key=crossref.5f4846d96e96da6689b641740716977c.

[45] N. C. Logan, B. A. Grierson, S. R. Haskey, S. P. Smith, O. Meneghini, and D. Eldon, Preprint pp. 1–17 (2017), URL message:{%}3CCAKNixhoASbPpgMU6E6kO82v59uDrQQYhhFCd5{_}NY3QZhqeEXhQ@mail.gmail.com{%}3E.

[46] B. A. Grierson, X. Yuan, M. Gorelenkova, S. Kaye, N. C. Logan, O. Meneghini, S. R. Haskey, J. Buchanan, M. Fitzgerald, S. P. Smith, et al., Fusion Sci. Technol. pp. 1–15 (2018), ISSN 1536-1055, URL https://www.tandfonline.com/doi/full/10.1080/15361055.2017.1398585.

[47] J. Candy and R. E. Waltz, J. Comput. Phys. **186**, 545 (2003), URL http://linkinghub.elsevier.com/retrieve/pii/S0021999103000792.

[48] W. A. Hornsby, C. Angioni, Z. X. Lu, E. Fable, I. Erofeev, R. M. McDermott, A. Medvedeva, A. Lebschy, A. G. Peeters, and t. A. U. Team, Nucl. Fusion **58**, 56008 (2018), URL http://stacks.iop.org/0029-5515/58/i=5/a=056008?key=crossref.b2524c54ba970acb71d92310c443f31a.

[49] C. L. Rettig, T. L. Rhodes, J. N. Leboeuf, W. A. Peebles, E. J. Doyle, G. M. Staebler, K. H. Burrell, and R. A. Moyer, Phys. Plasmas **8**, 2232 (2001), URL http://scitation.aip.org/content/aip/journal/pop/8/5/10.1063/1.1362537.

[50] J. Citrin, H. Arnichand, J. Bernardo, C. Bourdelle, X. Garbet, F. Jenko, S. Hacquin, M. J. Pueschel, and R. Sabot, Plasma Phys. Control. Fusion **59**, 64010 (2017), URL http://iopscience.iop.org/article/10.1088/1361-6587/aa6d1d.

[51] B. Grierson, K. Burrell, W. Solomon, R. Budny, and J. Candy, Nucl. Fusion **53**, 063010 (2013), ISSN 0029-5515, URL http://stacks.iop.org/0029-5515/53/i=6/a=063010?key=crossref.ef216c6db30f2d140d55fef091efb8e1.

[52] W. M. Solomon, K. H. Burrell, R. Andre, L. R. Baylor, R. V. Budny, P. Gohil, R. J. Groebner, C. T. Holcomb, W. A. Houlberg, and M. R. Wade, Phys. Plasmas **13**, 56116 (2006).

[53] E. A. Belli and J. Candy, Plasma Phys. Control. Fusion **50**, 95010 (2008), URL http://iopscience.iop.org/0741-3335/50/9/095010.

[54] N. T. Howard, A. E. White, M. L. Reinke, M. Greenwald, C. Holland, J. Candy, and J. R. Walk, Nucl. Fusion **53**, 123011 (2013), URL http://stacks.iop.org/0029-5515/53/i=12/a=123011?key=crossref.8630cc7fddefec7fcfd363bc741f0326.

[55] G. M. Staebler, J. E. Kinsey, and R. E. Waltz, Phys. Plasmas **12**, 102508 (2005).

[56] G. M. Staebler, J. E. Kinsey, and R. E. Waltz, Phys. Plasmas **14**, 55909 (2007).

[57] J. Candy, C. Holland, R. E. Waltz, M. R. Fahey, and E. A. Belli, Phys. Plasmas **16**, 60704 (2009).

[58] C. Chrystal, B. Grierson, G. Staebler, C. Petty, W. Solomon, J. DeGrassie, K. Burrell, T. Tala, and A. Salmi, Phys. Plasmas **24** (2017), ISSN 10897674.

[59] R. Pinsker, M. Austin, D. Ernst, A. Garofalo, B. Grierson, J. Hosea, T. Luce, A. Marinoni, G. McKee, R. Perkins, et al., EPJ Web Conf. **87**, 02003 (2015), ISSN 2100-014X, URL http://www.epj-conferences.org/10.1051/epjconf/20158702003.

[60] W. X. Wang, Z. Lin, W. M. Tang, W. W. Lee, S. Ethier, J. L. V. Lewandowski, G. Rewoldt, T. S. Hahm, and J. Manickam, Phys. Plasmas **13**, 92505 (2006).

[61] R. E. Waltz, G. M. Staebler, and W. M. Solomon, Phys. Plasmas **18**, 42504 (2011), URL http://scitation.aip.org/content/aip/journal/pop/18/4/10.1063/1.3579481.

[62] W. Wang, B. Grierson, S. Ethier, J. Chen, E. Startsev, and P. Diamond, Phys. Plasmas **24** (2017), ISSN 10897674.

[63] Ö. D. Gürcan, P. H. Diamond, T. S. Hahm, and R. Singh, Phys. Plasmas **14**, 42306 (2007), URL http://scitation.aip.org/content/aip/journal/

pop/14/4/10.1063/1.2717891.

[64] W. X. Wang, T. S. Hahm, S. Ethier, L. Zakharov, and P. H. Diamond, Phys. Rev. Lett. **106**, 85001 (2011), URL http://prl.aps.org/abstract/PRL/v106/i8/e085001.

[65] Ö. D. Gürcan, P. H. Diamond, P. Hennequin, C. J. McDevitt, X. Garbet, and C. Bourdelle, Phys. Plasmas **17**, 112309 (2010), URL http://scitation.aip.org/content/aip/journal/pop/17/11/10.1063/1.3503624.

[66] Z. X. Lu, E. Fable, W. A. Hornsby, C. Angioni, A. Bottino, P. Lauber, and F. Zonca, Phys. Plasmas **24**, 042502 (2017), ISSN 1070-664X, URL http://aip.scitation.org/doi/10.1063/1.4978947.

[67] P. Rodriguez-Fernandez, A. White, N. Howard, B. Grierson, G. Staebler, J. Rice, X. Yuan, N. Cao, A. Creely, M. Greenwald, et al., Phys. Rev. Lett. **120** (2018), ISSN 10797114.